Energetics, skeletal dynamics, and long-term predictions on Kolmogorov-Lorenz systems

V. Pelino* and F. Maimone†

Italian Air Force, CNMCA, Aeroporto "De Bernardi," Via di Pratica Di Mare, I-00040 Pratica di Mare (Roma) Italy

(Received 29 May 2007; revised manuscript received 15 August 2007; published 17 October 2007)

We study a particular return map for a class of low-dimensional chaotic models called Kolmogorov-Lorenz systems, which received an elegant general Hamiltonian description and also includes the famous Lorenz-63 case, from the viewpoint of energy and Casimir balance. In particular, a subclass of these models is considered in detail, precisely those obtained from the Lorenz-63 by a small perturbation on the standard parameters, which includes, for example, the forced Palmer-Lorenz case. The paper is divided into two parts. In the first part the extremes of the mentioned state functions are considered, which define an invariant manifold, used to construct an appropriate Poincaré surface for our return map. From the "experimental" observation of the simple orbital motion around the two unstable fixed points, together with the circumstance that these orbits are classified by their energy or Casimir maximum, we construct a conceptually simple skeletal dynamics valid within our subclass, reproducing quite well the Lorenz cusp map for the Casimir maximum. This energetic approach sheds some light on the "physical" mechanism underlying the regime transitions. The second part of the paper is devoted to an investigation of a type of maximum energy-based long-term predictions, by which knowledge of a particular maximum energy "shell" amounts to knowledge of the future (qualitative) behavior of the system. It is shown, in this respect, that a local analysis of predictability is not appropriate for a complete characterization of this behavior. A perspective on the possible extensions of this type of predictability analysis to more realistic cases in (geo)fluid dynamics is discussed at the end of the paper.

DOI: 10.1103/PhysRevE.76.046214 PACS number(s): 05.45.Ac, 47.52.+j

I. INTRODUCTION

A largely studied model exhibiting chaos has been that obtained by Lorenz in 1963 [1] by a drastic truncation of the fluid-dynamics equations as applied to the problem of thermal convection. Since then, Lorenz equations have been derived and applied in a wide variety of contexts [2–6].

Particularly, it was originally thought of for meteorological applications, where low-dimensional models of this type ([7], and references therein) still form the basis of our current understanding and intuition about atmospheric and climate nonlinear dynamics. In this respect, such models have been used to infer the limits of atmospheric predictability [8], and the characteristic time of exponential divergence between two nearby trajectories in phase space has been estimated to have the value of about 10–15 days, at least as far as one is concerned with synoptic-scale disturbances. This conclusion about the existence of a predictability horizon for the atmosphere has been achieved from very different approaches. A remarkable classical argument, for instance, is based on topological fluid dynamics and was carried out by Arnold in 1950 (see Ref. [9]), who estimated the characteristic time for a two-dimensional (2D) ideal fluid on a torus having the Earth's size to be of the order of 2 weeks, well before the advent of massive computer capabilities applied in this field.

Nevertheless, it was pointed out that predictability—i.e., error growth—strongly depends on the space and time scales considered (see, for example, Refs. [7,10]). In fact, it turns out that if one is concerned, instead, with the coarser-grained atmospheric flows generally known as weather regimes, which capture the atmospheric variability comprised between 10 and 100 days, predictability of state transitions is greatly enhanced, as shown, for example, by the use of statistical autoregressive methods [11,12]. In particular in Ref. [12], an atmospheric three-level model based on the barotropic vorticity equation has been used to study these transitions. A parameter—i.e., the exit angle from a given regime—has been suggested as a candidate predictor, and a comparison with a stochastic variant of the Lorenz model has been made. Results are encouraging, but detailed knowledge of the regimes boundaries is required, making the application of the method to real observations quite hard.

It is well known that thermofluid dynamical equations for ideal systems can be put in an elegant (noncanonical) Hamiltonian form [13,14]. While this formulation obviously adds nothing to the physics of the fluid systems considered, the main mathematical structures turns out to be much more clear in this approach. In particular, an infinite class of enstrophylike Casimir functions are easily identified, whose time variations are eventually due only to the action of dissipation and forcing mechanisms.

In this respect, it would be useful to handle the analysis with toy models, whose behavior can be completely understood, possessing the same mathematical structure as the real fluid dynamical equations.

On the one hand, it is a quite general consequence of the model truncation necessary to solve numerically the equations, like the one employed in the simulation of the atmosphere for operational forecasting purposes (e.g., [15]), that the Hamiltonian form is not preserved in the resulting discrete system of (ordinary) differential equations.

On the other hand, it has recently been shown that an important class of 3D chaotic models, including Lorenz-63 and a (symmetric) variant of Lorenz-84 models, the so-called Kolmogorov-Lorenz systems, can indeed be equipped with a

*pelino@meteoam.it
†maimone@meteoam.it

natural geometrical group structure equivalent to that used in the infinite-dimensional case [11], which results in a rigorous Hamiltonian formalism [16,17].

The paper is organized as follows. In Sec. II the Hamiltonian formulation of Kolmogorov-Lorenz system is summarized and the related geometrical return maps introduced. Section III first focuses on the energetics of Lorenz-63, with a discussion of a more general (forced) case (Sec. III A); then, a skeletal dynamics is constructed, based on this energetics (Sec. III B). In Sec. IV the relation between energetics and predictability is investigated, starting from a study of linear instability (Sec. IV A) and continuing with a discussion of long-term predictions based on energy maxima (Sec. IV B). Section V is devoted to a proposal aimed at extending the connection found to more realistic fluid dynamical systems, while Sec. VI concludes the paper with a few final comments.

II. HAMILTONIAN FORMULATION AND GEOMETRICAL MAPS

The main peculiarity of the Lorenz-63 model consists in the following: for a suitable choice of the parameters, a chaotic macrodynamics can be identified, which consists of sudden and unpredictable transitions between two separate regions in phase space, which will be referred to as the left (Ψ_L) and right (Ψ_R) regions covering the attractor $\Psi = \Psi_L \cup \Psi_R$.

As can be easily shown [18], this macrodynamics can be characterized by a simple statistical law, using a new discrete-time map having a precise physical meaning.

On the other hand, it can be demonstrated that the Lorenz-63 system

$$\dot{x}_1 = -\sigma x_1 + \sigma x_2,$$

$$\dot{x}_2 = -x_1 x_3 + \rho x_1 - x_2,$$

$$\dot{x}_3 = x_1 x_2 - \beta x_3 \tag{1}$$

is not but a particular example of a much wider class of models with a well-defined geometrical interpretation, the so-called Kolmogorov-Lorenz equations, in which a clear distinction among Hamiltonian, dissipative, and forcing terms is made [16].

To be specific, the right-hand side of Eqs. (1) can be written as the sum of the Lie-Poisson brackets of the algebra of the SO(3) spatial rotation group and of a dissipation and forcing term (from hereon the Einstein summation convention is used),

$$\dot{x}_i = \{x_i, H\} - \Lambda_{ij} x_j + f_i \quad (i = 1,2,3), \tag{2}$$

assuming the following gyrostatlike Hamiltonian:

$$H = \frac{1}{2}\Omega_{ik} x_i x_k + h_k x_k, \tag{3}$$

where $\mathbf{\Omega} = \mathrm{diag}(2,1,1)$, $\mathbf{\Lambda} = \mathrm{diag}(\sigma,1,\beta)$ is the dissipation matrix, $\mathbf{h} = (0,0,-\sigma)$ an axisymmetric rotor, and $\mathbf{f} = (0,0,-\beta(\rho+\sigma))$ an external forcing. An important result of this formalism is that there is not chaotic behavior in the system for $\mathbf{h} = \mathbf{0}$.

Here the brackets represent the algebraic structure of the Hamiltonian part of the system described by the function H and a cosymplectic form $\mathbf{J}$ [19] defined by

$$\{F, G\} = J_{ik} \partial_i F \partial_k G. \tag{4}$$

For a conservative system, in the local coordinates x_i, the Lie-Poisson equations read as

$$\dot{x}_i = \varepsilon_{ijk} x_j \partial_k H, \tag{5}$$

where the Levi-Cività symbol ε_{ijk} represents the constants of structure of the algebra $\mathbf{g} = \mathrm{so}(\mathbf{3})$ and the cosymplectic matrix assumes the form $J_{ik} = \varepsilon_{ijk} x_j$; in this formalism, $\mathbf{g}$ is endowed with a set of Poisson brackets characterized by Eq. (2) for functions $F, G \in C^\infty(\mathbf{g}^*)$.

Casimir functions C are given by the kernel of the set brackets (4)—i.e., $\{C, G\} = 0, \ \forall \ G \in C^\infty(\mathbf{g}^*)$; therefore, they represent the constants of motion of the Hamiltonian system, $\dot{C} = \{C, H\} = 0$.

In a geometrical language, these constants of motion define a foliation of the phase space [9], and motion takes place at the intersection of the ellipsoid $E: \frac{1}{2}\Omega_{ik} x_i x_k + h_k x_k = H$ with the sphere S^2 given by the Casimir $x_k x_k = C$, leading to Euler dynamics for the rigid body,

$$\mathbf{x}(t) \in \mathrm{E} \cap S^2. \tag{6}$$

In the general case of a dissipative-forced system [17], the dynamics is also constrained by (6), but in this case the two geometrical objects S^2 and E do expand and contract in a chaotic way, reaching a set of maximal and minimal values during their evolution. In particular, it is natural to consider the set of $\mathbf{x}(t)$ such that S^2 reaches a relative maximum or minimum radial value. This is given by imposing the simple condition $\dot{C}(t) = 0$, which using Eq. (2) reads as $-\Lambda_{ik} x_i x_k + f_i x_i = 0$ and defines an invariant ellipsoid, whereas the curve $\ddot{C}(t) = 0$ on this surface separates the maxima from the minima regions. Besides, the maximum distance of the points on the ellipsoid from the origin of the coordinates identifies, by construction, the radius of a sphere in which the attractor is entirely contained. Incidentally, these geometrical conditions can be used to verify the consistency of this type of numerical simulations.

Let us now specialize to the Lorenz case of Eq. (1). As is well known, for a suitable choice of parameters the solutions of Lorenz equations are given by chaotic trajectories revolving around the three unstable fixed points of Eq. (1). In Ref. [18] a clear geometrical method has been established to compute the frequencies of these chaotic oscillations.

Now, the dynamical condition $\dot{C}(t) = 0$ can be translated in geometrical terms by the requirement that points have to lie, after the translation $(x_1, x_2, x_3) \to (x_1', x_2', x_3') = (x_1, x_2, \sqrt{\rho} x_3 + \beta(\rho+\sigma)/2\sqrt{\rho})$, on the ellipsoid of rotation centered in the origin of coordinates:

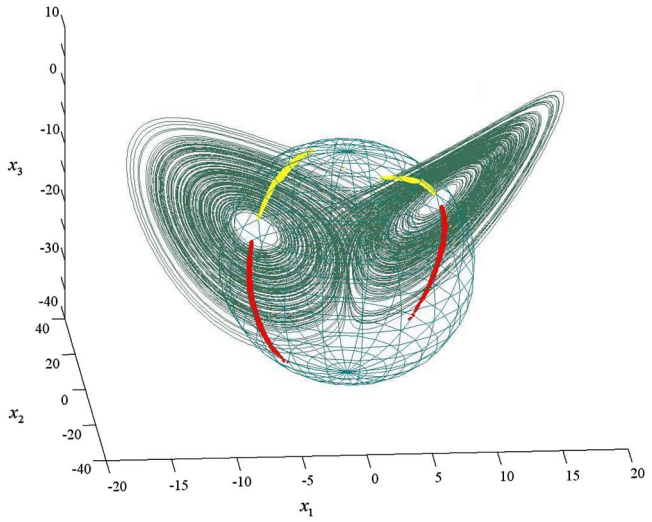

FIG. 1. (Color online) Ellipsoid of Casimir extremes intersecting the attractor in four regions, the two stripes in the semispace $x_2<0$ representing the set of maxima and the remaining two ($x_2>0$) the minima.

$$E_C: \sigma x_1'^2 + x_2'^2 + x_3'^2 = \left[\frac{\beta(\rho+\sigma)}{2\sqrt{\rho}}\right]^2, \tag{7}$$

which is a fixed manifold with respect to the chaotic motion on the attractor $\mathbf{x}'(t) \in \Psi$, with a fractal structure for Ψ. In this way it is natural to choose the Poincaré section for the Lorenz attractor as the intersection

$$\mathbf{x}'(t_k) \in \mathrm{E}_C \cap \Psi. \tag{8}$$

Such an intersection defines four symmetric regions on the ellipsoid E_C, representing the sets of max(C) and min(C) for the two lobes of Ψ, as shown in Fig. 1. Return maps for these points give the periods of rotation and revolution, respectively, about each lateral fixed point and about the central unstable point.

To fix the ideas let us concentrate on the first return map of one of the maxima—the left one, say. The spectrum of the return times depicted in Fig. 2 shows a definite band structure with a constant spacing separation, which can be interpreted as follows: starting from the bottom, the first band (index $n=0$) represents a single rotation in the left lobe, the second ($n=1$) corresponds to a semirotation in the left lobe followed by a complete rotation in the other lobe plus a semirotation in the starting lobe, etc.

So the nth band corresponds to n complete rotations in the right lobe and return.

The constant spacing separation along the time vertical axis amounts to a characteristic time of $\tau_0 \approx 0.66$ units and can be defined as the spacing between the barycenters of the point distributions of the bands.

Because of the reflection symmetry $x_i \to -x_i$, $i=1,2$, in Eq. (1) (the same holds for the variables x_i'), the identical statistical behavior can be verified, taking as starting point the maximum on the right side—analogously for the minima, which present slightly different statistics.

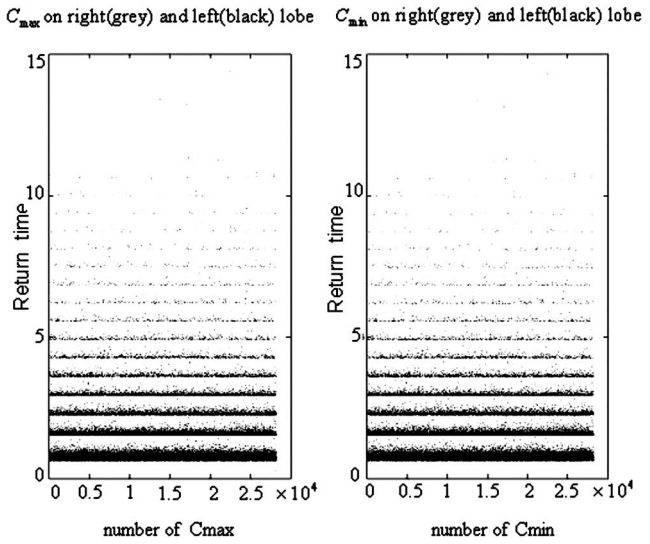

FIG. 2. Band structure of the return times. In the horizontal axis the ordinal number of $C_{\max}$ and $C_{\min}$ is found in the simulation. Because of the reflection symmetry, point distributions in the bands for the right and left side overlap quite well, so that they are not so well distinguishable in the figure.

It should be stressed that even if a similar result can be expected also for other suitably chosen Poincaré sections, the regions of extrema on the invariant ellipsoid correspond to a very natural choice within our class of models, being automatically defined for all of them. Also, we point out the identical structure of the map of Casimir maxima relative to the standard x_3 Lorenz cusp map [see Fig. 11(a)]. Moreover, in order to distinguish the jumps in the time sequence $C_n \in \max(C)$, $n=1,2,\ldots$, between Ψ_L and Ψ_R, it would be more natural to consider the regime-selective map for the set of values $D_n=\sigma(x_1)C_n$, where $\sigma(x_1)=+1$ for $x_1>0$ and $\sigma(x_1)=-1$ for $x_1<0$. In the following we will also consider the discrete map of maximum Casimir referring to a single lobe.

III. ENERGETICS OF LORENZ-63

We are now going to consider the behavior of the system from the viewpoint of the energy and Casimir functions.

A. Energy balance between forcing and dissipation

As follows immediately from Eqs. (2) and (3), even if energy is not conserved, the energy gain in a given finite trajectory on the attractor should be equal to the time integral of the sum of the injection power and of the dissipation power along the track,

$$E(t_2) - E(t_1) = \int_{t_1}^{t_2} \dot{H}\, dt = -\int_{t_1}^{t_2} \Lambda_{ij}(\Omega_{ik}x_j + h_k)x_k dt + \int_{t_1}^{t_2} f_i(\Omega_{ik}x_k + h_i)dt. \tag{9}$$

Since the (natural) forcing injection and the dissipation loss vary in a different way on the attractor, being functions, re-

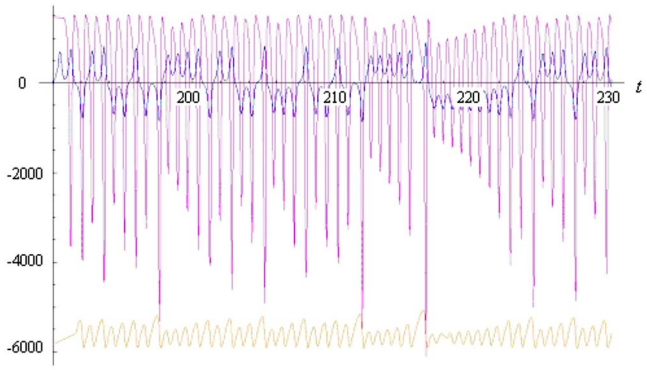

FIG. 3. (Color online) Time variation of total energy (bottom curve), forcing-dissipation power (highest amplitude oscillations in the figure), and x_1 coordinate. The variables are represented not in scale; in particular, the plotted functions are, respectively, $E(t)-6000$, $\dot{E}(t)$, and $50x_1$.

spectively, linear and quadratic of the phase-space coordinates, the energy balance (9) acts to constrain phase-space points on well-defined paths on the attractor.

The three curves depicted (not in scale) in Fig. 3 represent the total energy (bottom curve), the forcing-dissipation power (highest amplitude oscillations in the figure), and the x_1 coordinate. From the analysis of these curves it emerges that, from an energetic viewpoint, the system soon after a passage from the companion lobe tends to acquire energy around the unstable central fixed point, where the (positive) forcing pushes the systems towards higher maximum energies, which are reached on a peripherical side of the lobe, as can be seen from Fig. 4, in which energy injection per unit length,

$$\dot{E}/\|\mathbf{v}\|, \tag{10}$$

is represented, where $\mathbf{v}=(\dot{x}_1,\dot{x}_2,\dot{x}_3)$ is the velocity field.

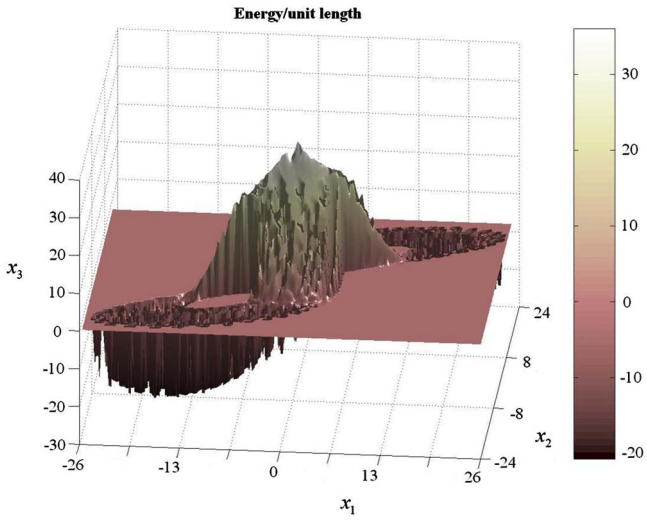

FIG. 4. (Color online) Energy acquired per unit length represented in the plane (x_1,x_2) by time averaging on the x_3 direction.

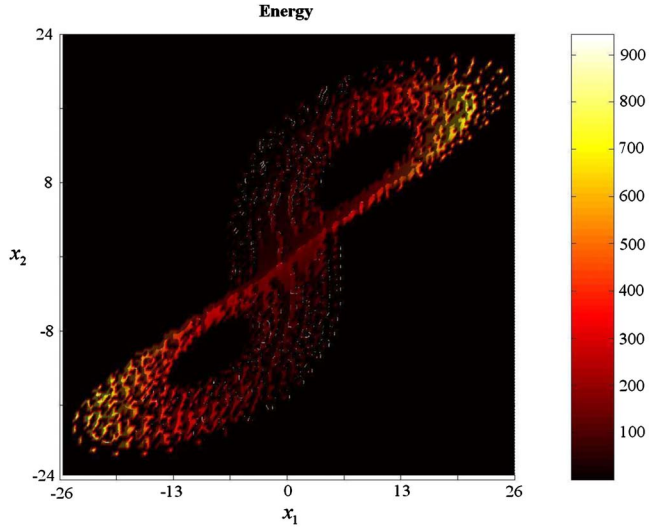

FIG. 5. (Color online) Total energy represented in the plane (x_1,x_2) by time averaging on the x_3 direction.

After the energy maximum has been reached, dissipation becomes more and more important along the system's trajectory, causing energy loss. If this loss exceeds a threshold, the energy gain near the center of the attractor is not sufficient to sustain another oscillation around the fixed point of the current lobe and the system is *pushed* into the other regime. Otherwise, the system is allowed to experience another turn within the same lobe along a more external trajectory and so on. It is then possible that the system's state performs n turns within a given lobe, experiencing at each successive step more and more external turns around the fixed point. As is shown in Fig. 5, because of the greater energy gain near the attractor's center, it happens that the very internal trajectories acquire much less energies when passing there than more external ones. At the same time the former ones suffer only for a small dissipation in each turn. As a result, the small amount of energy acquired allows for a small radius increment of the trajectory itself in a complete turn. This fact, on the other hand, leads to a higher number of consecutive turns inside the given lobe, up to the "critical" one, in which dissipation becomes unsustainable and the system "decays" into the other regime. This is the qualitative explanation of the cusp form of the Lorenz map from an energetic viewpoint. Incidentally, it can be verified that the same type of maps can be obtained for both energy and Casimir maxima.

Moreover, it results from a simple inspection of Fig. 3 that the most external orbits above the critical radius end up in very internal orbits on the other lobe, which means a large number of consecutive turns within this latter. This circumstance strongly suggests that maximum energies could be linked to the number of turns the system will perform on the other lobe—i.e., to the long-term behavior of the system, as we will verify later.

Finally, in order to give the flavor of the generality of the present approach, we briefly consider the case studied in Ref. [6], in which a regime-selective behavior is obtained through the introduction of a further (weak) forcing in the x_1 and x_2 equations, parametrized by the angle ϑ. In a more general case, assuming a forcing $\mathbf{f}$,

$$f_1 = f \cos\varphi \cos\vartheta,$$

$$f_2 = f \cos\varphi \sin\vartheta,$$

$$f_3 = f \sin\varphi, \tag{11}$$

where $f=-\beta(\rho+\sigma)$, it is easy to show that for $\varphi \neq \frac{\pi}{2}$ there is a symmetry breaking in the Lorenz equations, leading to different statistics and predictability on the two lobes. What happens, from an energetic viewpoint, is that the introduction of this additional forcing modifies the central "hill" of Fig. 4 (with a simultaneous small displacement of the lateral unstable points, the form of the attractor remaining essentially the same) in such a way that it becomes asymmetric—i.e., a bit more pronounced (with the values set in Ref. [6]) on a lobe than on the other—the dissipation term remaining the same. In such a way, on the lobe in which it is more pronounced, internal orbits are forced to acquire more rapidly energy, so that the representative point is pushed, on the average, a bit faster towards the opposite regime. Conversely, for an internal orbit originating in this latter, maximum-energy growth is decelerated, so that the (mean) residence time of the representative point in that regime is increased. This gives rise to the observed difference in the pair distribution function (PDF) on the two lobes.

B. Orbits and skeletal dynamics

It is an "experimental" observation that, starting from the Lorenz type of the Kolmogorov-Lorenz systems settled with the original Lorenz parameters ($\sigma=10$, $\rho=28$, $\beta=\frac{8}{3}$), for a wide range of variations around them, within the chaotic regime, some peculiar dynamical properties are kept robust (see, e.g., the case of Ref. [6]). These properties refer, for example, to the fractal dimension of the attractor, which may preserve approximately the value of $d \approx 2.06$, and to the macrodynamics, which remains qualitatively unchanged.

Moreover, it is important to note that the sets of maximum energies have a natural ordering, i.e., maximum energies are growing functions of the orbit radius in each lobe (see Fig. 6). Note that this property does not hold for the minimum ones.

Then, apart from the fine-grained structure, the fractal attractor can be geometrically approximated by a two-dimensional manifold. To be specific we consider two distinct surfaces, one for each wing of the attractor, which glue together at the points in which the lines, originating in a given region, enter the opposite wing. We have obtained such surfaces by interpolating 10^3 uniformly distributed points in each lobe, with two third-order polynomials in the variables x_1 and x_2, $z(x_1,x_2)$. So the left and right wings are geometrically described, respectively, by the metrics (induced by the usual Euclidean 3D metric of the phase-space) g_L and g_R.

In this setting, of course, the fractal regions of points of maximum energy are reduced to lines, being the intersections between the attractor surfaces and the invariant energy ellipsoid.

On the basis of the above "experimental observations" we construct our skeletal dynamics by making the following assumptions.

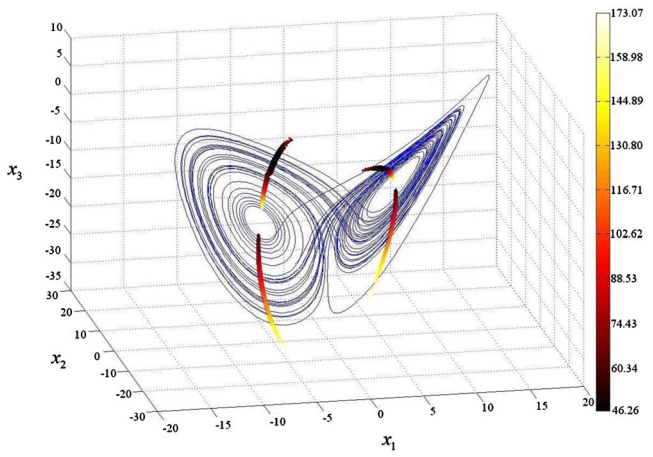

FIG. 6. (Color online) The ordered sets of Casimir maxima (the two stripes in the semi-space $x_2<0$) and minima (the remaining stripes, with $x_2>0$) are displayed on the attractor. Maxima are monotonic along the stripes, growing from the internal orbits to the external ones, while minima are not.

(i) The dynamics takes place on a two-dimensional manifold, a union of the two surfaces described above.

(ii) The basic geometrical elements of the trajectories are (a) circles (in the metric g) around the two lateral fixed points and (b) lines connecting circles on the two lobes.

(iii) Each circle, or orbit, intersects the curve of the energy maxima at a certain point. Then the next orbit is defined via the energy (forcing+dissipation) acquired in a complete turn in such a way that it will intersect the curve at a new point whose energy corresponds to the acquired energy added to the previous maximum [see Fig. 7(b)].

(iv) When the energy acquired within one orbit happens to be negative, the orbit itself is not completed, and at a certain point the motion is switched to a tangent line, until it reaches the other wing; from this moment on, the motion continues on the orbit passing through the crossing point and the cycles restart on the other "wing;" the switching point is determined in a self-consistent way by requiring that the energy acquired along the segment connecting the two lobes amount to the energy difference between the end points.

From these rules we will derive a number of consequences.

We start from the "forecast" of the number of turns the representative point will experience within the starting lobe and in the successive one soon after we have detected an energy maximum E_0 at a certain instant.

The number of turns made within the starting lobe is the maximum n such that

$$\oint_{\Gamma_n} \frac{\dot{H}}{\|\mathbf{v}\|} ds \geq 0, \tag{12}$$

where the line integral is performed along the nth orbit Γ_n, while the maximum energy acquired in lobe $L(R)$ is given, in an explicit, form by

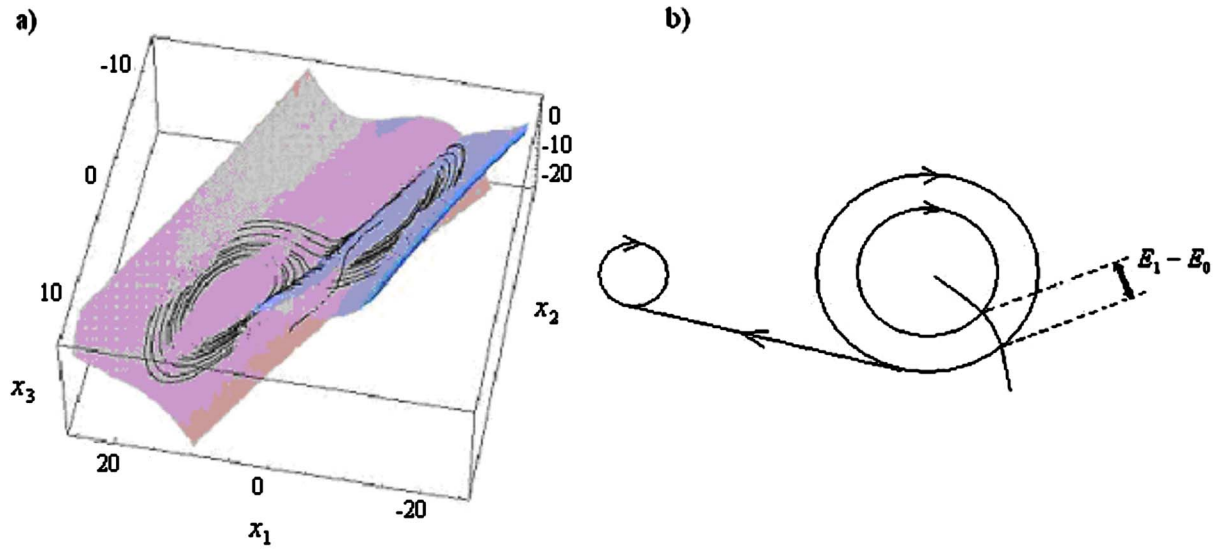

FIG. 7. (Color online) (a) Connecting surfaces obtained by interpolating 10^3 points for each wing using two third-degree polynomials in the variables x_1 and x_2, $z(x_1,x_2)$: $A+Bx_1+Cx_1^2+Dx_1^3+Ex_2+Fx_1x_2+Gx_1^2x_2+Hx_2^2+Ix_1x_1^2+Lx_2^3$, with $A=-22.95$, $B=5.25$, $C=-0.62$, $D=0.03$, $E=-3.31$, $F=0.76$, $G=-0.05$, $H=-0.21$, $I=0.03$, and $L=0.01$ for the right side and the polynomial obtained from this latter by reversing the coordinates for the left side. (b) Schematic view of the orbits intersecting the curve of energy maxima.

$$E_n = E_0 + \sum_{i=1}^{n} \oint_{\Gamma_i(\Gamma_{i-1})} \frac{-\Lambda_{kj}(\Omega_{kk}x_k+\omega_k)x_j + f_k(\Omega_{kk}x_k+\omega_k)}{\sqrt{\sum_{i=1}^{3}[\{x_i,H\}-\Lambda_{ij}x_j+f_i]^2}} ds. \tag{13}$$

The line element in the equations above is

$$ds = \sqrt{g_{ij}^{L(R)}(x_1,x_2)dx_i dx_j},$$

$$g_{i,j}^{L(R)} = \begin{pmatrix} [1+\partial_{x_1}z]^2 & (\partial_{x_1}z)(\partial_{x_2}z) \\ (\partial_{x_1}z)(\partial_{x_2}z) & [1+\partial_{x_2}z]^2 \end{pmatrix}. \tag{14}$$

Now, using this "theory of orbits," we compute the successive (maximum) energy levels starting from a given maximum. The result is depicted in Fig. 8, against the true cusp map of maxima.

Given the good correspondence of the skeletal model points with the true Lorenz cusp map, we can conclude that our theory of orbits captures the gross features of the dynamics. Since each orbit is, by definition, unambiguously associated with a maximum of energy, we can conclude that this quantity is a good control parameter for the system's behavior.

It should be stressed that the present skeletal model is only intended to give an energetic justification of the Lorenz cusp map; i.e., for a given Casimir maximum, it furnishes the approximate next value of this latter, the full chaotic dynamics remaining, in any case, not reproducible by substituting the fractal set of the attractor with a regular surface.

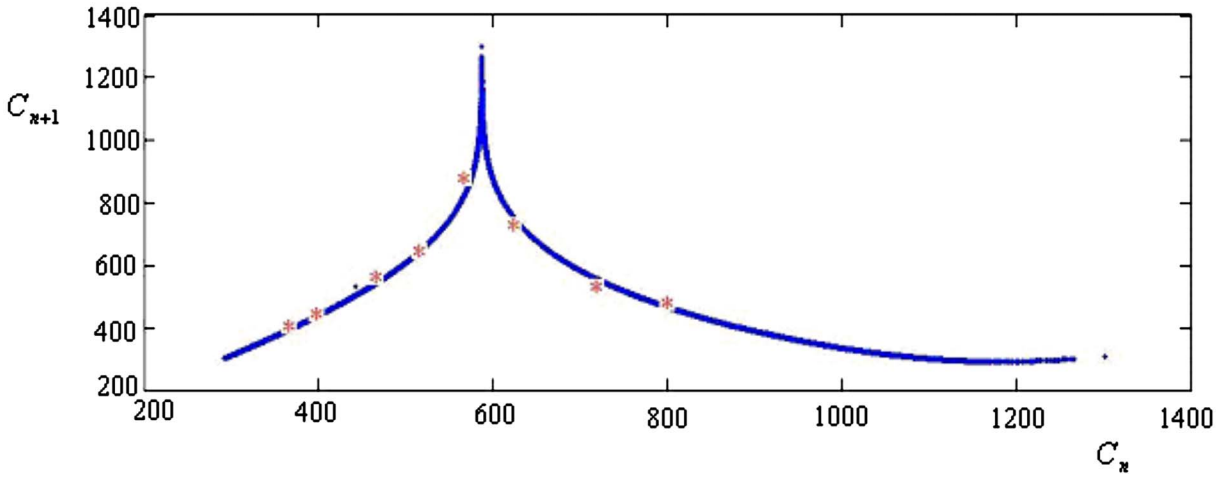

FIG. 8. (Color online) Lorenz cusp map points (dots) for the Casimir maximum plotted against the experimental map (solid line).

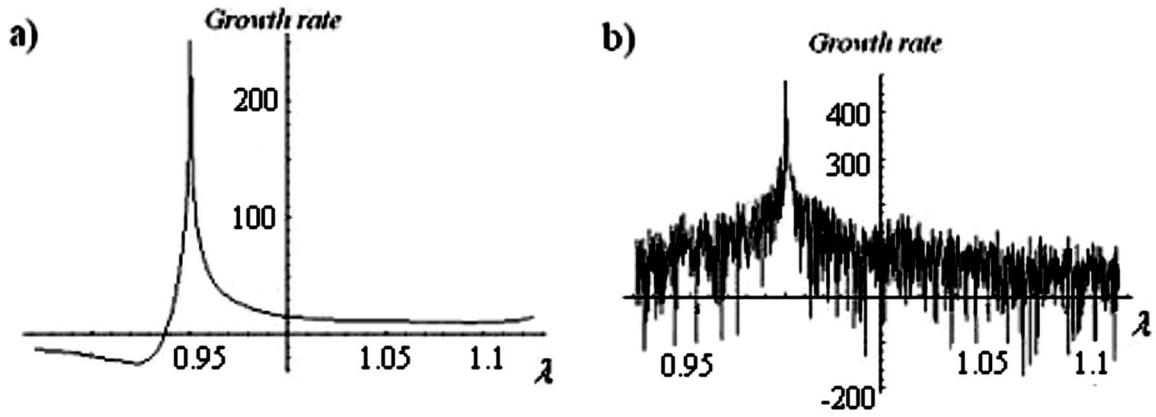

FIG. 9. Growth rate calculated along the curve of maxima (parametrized by the affine parameter λ) going from the internal orbits (lower values of λ) to the external ones and taking the initial perturbations along the curve (a) and in the (1,1,1) direction in the phase space (b).

IV. ENERGETICS AND PREDICTABILITY

In this section we discuss the connection between energetics and predictability. We analyze this latter first in the "local" (linear) approach; then, we pass to a longer-term predictability analysis based on nonlinear evolution and to an interesting use of energy and Casimir maxima as control variables to infer the qualitative future behavior of the system.

A. Local instability by linear perturbation analysis

Let us calculate the analytic expression of the perturbation growth rate in the natural Euclidean metric as a function of coordinates, and with a parametric dependence on the vector of the initial perturbation, on the (small) time interval of the evolution considered.

To be specific, we consider the evolution of two nearby initial points x_i^0 and $\tilde{x}_i^0$. The dynamical equation for the difference is

$$\frac{d}{dt}(x_i - \tilde{x}_i) \equiv \frac{d\delta x_i}{dt} = \{\delta x_i, H\} - \Lambda_{ij}(\delta x_i), \tag{15}$$

from which, considering a sufficiently small time interval Δt, we get the equations for $\delta x_i(\Delta t)$:

$$\delta x_i(\Delta t) \approx \delta x_i^0 + \Delta t[\Omega_{kj}\varepsilon_{ijk}(x_k x_j - \tilde{x}_k\tilde{x}_j) + h_k\varepsilon_{ijk}\delta x_j(\Delta t) - \Lambda_{ij}\delta x_j(\Delta t)] \equiv \delta x_i^0 + \hat{M}_{ij}\delta x_j(\Delta t). \tag{16}$$

Solving this linear system with respect to $\delta x_i(\Delta t)$, the perturbation vector growth rate can be conveniently expressed by [15]

$$\gamma = \frac{1}{\Delta t}\ln\frac{\sum_{k=1}^{3}\delta x_k^2(\Delta t)}{\sum_{k=1}^{3}\delta x_k^{02}} = \frac{1}{\Delta t}\ln\frac{\sum_{k=1}^{3}(\det\|\hat{M}_{ij}^{(k)}\|/\det\|\hat{M}_{ij}\|)^2}{\sum_{k=1}^{3}\delta x_k^{02}}, \tag{17}$$

where the matrix $\|\hat{M}_{ij}^{(k)}\|$ is obtained from $\|\hat{M}_{ij}\|$ by substituting the kth column with the vector $(\delta x_1^0, \delta x_2^0, \delta x_3^0)^T$.

In Fig. 9 the growth rate is depicted along the curve of maximum energies of the skeletal attractor setting a time step $\Delta t = 0.02$ and choosing the initial errors $\delta x_i^0 \approx O(10^{-1})$, respectively, along the curve and in the fixed direction (1,1,1). The result is that there is only one evident maximum, corresponding to an energy E and a Casimir C, and for which, conversely, local predictability reaches its minimum. This maximum identifies precisely the critical point of regime transition on the line of maxima. Rapid oscillations in the second case are only due to the fact that one of the initial conditions (in each couples of initial conditions considered) in general does not belong to the attractor. We point out that the long-term predictability we will be concerned with cannot be identified by means of a (local) linear analysis of instability in the regions of maxima. In fact, as we will see in the following, a new type of long-term predictability emerges, in which knowledge of the starting energy shells above the critical point identifies precisely the number of turns, and then the mean time the opposite regime will last.

B. Long-term predictions using energy maxima

We have already seen and interpreted the band structure of the return times of our Poincaré map.It is interesting that, when considering the return times as a function of the energy or Casimir maximum, we find the ordered structure depicted in Fig. 10. Starting from a Casimir maximum on a given lobe, the system's state will wander around through the attractor and then, after a certain time, it will return to another maximum on the same lobe. The map of Fig. 10 contains the return times plotted against the Casimir as obtained in a long-time integration of 40×10^6 calculation steps. This emerging band structure (the same holds true for the energy) can be easily linked to the band structure of Fig. 2 and interpreted in an analogous way: the first band (from the left) corresponds to a turn within the starting lobe, while the $(n+1)$th band corresponds to n turns on the other lobe and return.

So, in other words, to a certain maximum Casimir range it corresponds to a precise return time, so that knowledge of this quantity, according to the discussion above, amounts to knowledge of the number of turns on the other lobe.

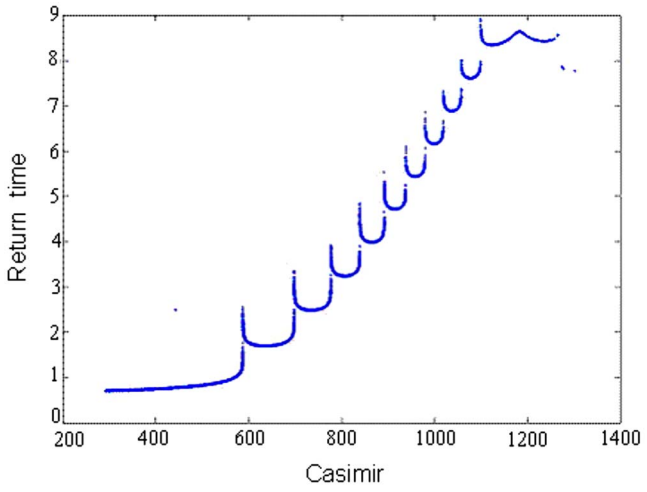

FIG. 10. (Color online) Return times as a function of Casimir maximum.

An interesting question is whether a given Casimir maximum also determines its next map iteration value, in such a way that one could be able, not only to forecast the next number of turns, but also the successive ones and so on, with the possibility of encoding a complete symbolic dynamic description of the system in an ordered sequence of the number of turns alternatively performed on the two lobes.

Also, we can look at our system as a black box, whose input is the entrance energy—i.e., an initial maximum of energy on a given lobe—and the output is the energy maximum on the same lobe when the system is back. Figure 11 shows the map of Casimir maximum on a given lobe—for example, the right one, $C^r_{n+k}=f(C^r_n)$ (the label r is to stress the fact that we are considering here the map connecting Casimir maxima only at right). It is immediate to note that to a little uncertainty ΔC^r_n in the entrance Casimir maximum it corresponds, in general, a greater uncertainty ΔC^r_{n+k} in the exit Casimir maximum. Moreover, the ratio $\Delta C^r_{n+k}/\Delta C^r_n$

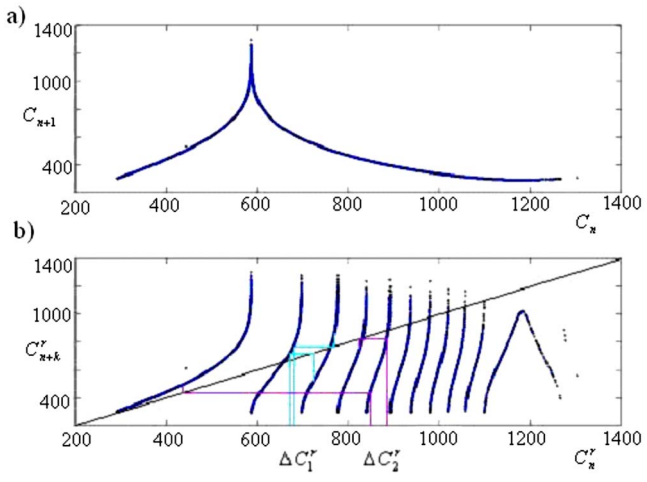

FIG. 11. (Color online) Lorenz cusp map for the Casimir maximumn (a). Casimir maximum on the right side, C^r_{n+k}, as a function of the previous Casimir maximum on the same side after k–turns, C^r_n (b).

$\approx \partial f/\partial C^r_n$ is, on the average on the bands, a growing function of the band index i, up to $i=10$.

In Fig. 11(b) two examples are considered. In the first, starting with the uncertainty ΔC^r_1 of the right lobe maximum, the system comes back at the next passage with a greater uncertainty, but with the Casimir range extremes still lying on the same band (the third one), meaning that after the subsequent jump the number of turns is still predictable.

In the second example, instead, the uncertainty ΔC^r_2 propagates in such a way that at the first passage the number of turns on the other lobe is precisely determined to be 4, but after the following transition this number is uncertain, ranging from 0 to 3.

Now, taking the set of maximum-energy points comprised within the extremes of a band, we can consider the flux tube determined by the dynamics in a neighborhood of this set. We will refer later on to these (local) fux tubes as to energy or Casimir shells.

We will now perform an ensemble long-term prediction to test, in particular, the sensitivity of a region enclosed in a given energy shell to the future behavior of the system, in comparison with the sensitivity of a somewhat other region on the attractor having the same phase-space extension (in the natural Euclidean metric). Alternatively we could have used the metric defined by energy and Casimir maxima themselves.

To be specific, consider a series of numerical experiments. In each one we take two sets of points, both belonging to the attractor and contained in the intersection of two equal spherical shells, the former contained within a given Casimir shell, the latter centered about a random point on the attractor. Then we let the two sets evolve. The intersection of the two spherical shells with the quasi-2D attractor approximately defines two coronas. We choose their internal and external radius in such a way that the first corona is entirely contained within a shell. The choice of external radius, on the other hand, is somewhat arbitrary, and it is only justified by the need of avoiding, as far as possible, the "noise," due to very nearby points, which are expected to have in a natural way a similar future behavior in our comparison experiment.

Two such experiments are illustrated in Figs. 12 and 13, respectively, for the case of an initial set chosen in a shell of Casimir maximum and centered in a random point on the attractor. It can be noticed that in the first case all the trajectories, after the transition, perform five turns on the other side, while in the second case they rapidly diverge. In the latter case this fact can be accounted for by noticing that the first Casimir maximum associated with the different trajectories is characterized by a wide spreading of values.

Here the operating principle is that two-nearby trajectories in the bulk of a lobe, the most densely occupied and internal part of it, can belong to really different histories, arriving within the lobe at maximum energy values corresponding to far distant away energy shells. Otherwise, in the opposite case, they may belong to trajectories ending in the same shell, this latter condition ensuring a similar future behavior.

Besides, it should be stressed that there are cases in which the random corona considered on the attractor results in a

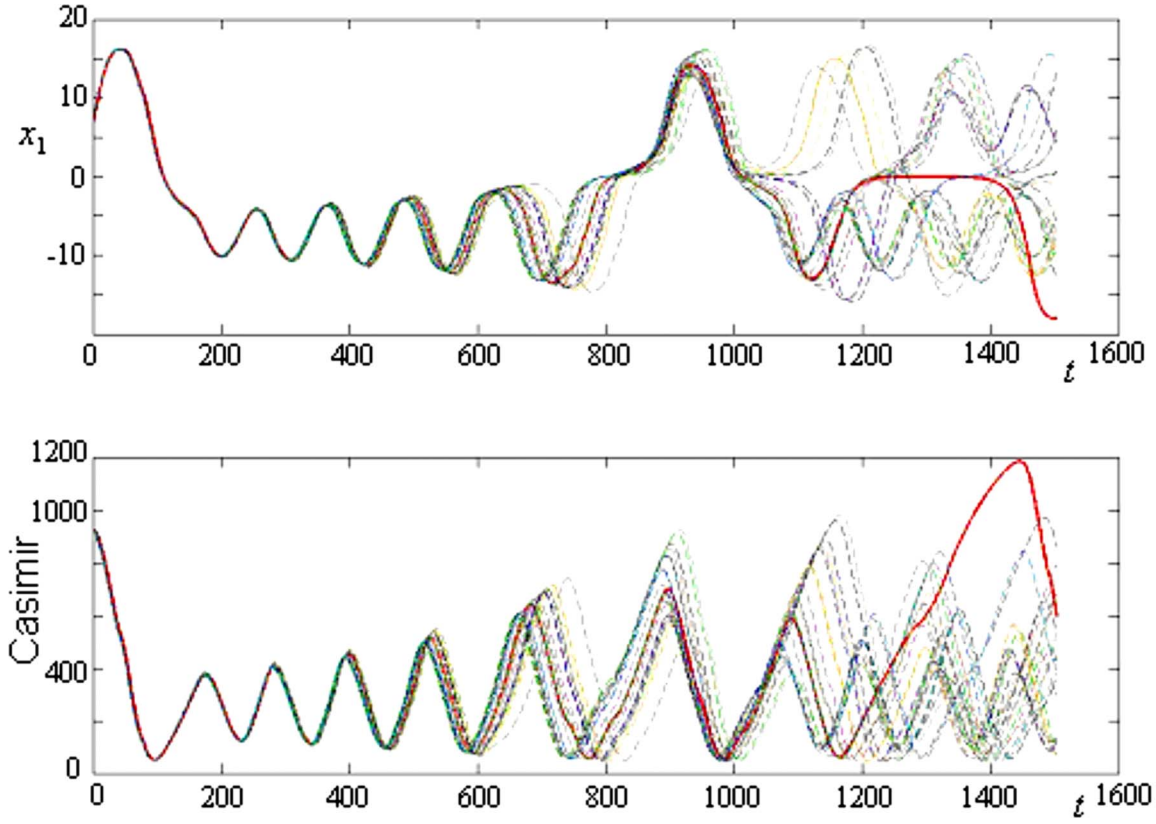

FIG. 12. (Color online) Evolution of x_3 (upper panel) and Casimir maximum (lower panel) starting from several initial conditions, different from each one but belonging to the same Casimir shell.

good predictability; i.e., all the trajectories starting from it are found to experience the same number of turns after the regime transition, and even later, after the subsequent transition, the predictability of this number can also be quite good. In Fig. 14 is shown a case like that, choosing a different point on the attractor. Again we can see that predictability is controlled by the Casimir maximum. In fact, the first maximum shows a very small dispersion around a relatively low value, and as a consequence most of the trajectories experience four tours in the negative-x regime, while the remaining ones only three. Things began to be worse with respect to predictability in the subsequent jump, which can be foreseen by the great dispersion of the previous Casimir maximum in the high values range. Still we conclude that future behavior is better foreseen at the particular moment in which the system reaches a maximum value of the control Casimir function.

V. PERSPECTIVES ON POSSIBLE EXTENSIONS TO MORE REALISTIC FLUID-DYNAMICAL SYSTEMS

The Hamiltonian description of the Kolmogorov-Lorenz systems and the construction of the invariant ellipsoid of the energy and Casimir maxima, with the associated return map, can be easily generalized, at least formally, to the case of a real fluid. Let us consider, for example, the energy in a 3D homentropic fluid in a given spatial domain. In the ideal case the fluid dynamics can be completely described by the Hamiltonian

$$H[u,x] = \int\int\int da\left\{\frac{1}{2}u^2 + \varepsilon\left(\frac{\partial x}{\partial a}, \eta(a)\right) + \Phi(x)\right\}, \tag{18}$$

where u and x are, respectively, the velocity and coordinates of the fluid particles, a an arbitrary labeling of them satisfying the condition $da=d(\text{mass})$, ε the internal energy, Φ an external potential, and η the specific entropy [20]. The presence of a forcing and a dissipation can be accounted for by adding to the equation of motion the corresponding terms

$$\frac{Du}{Dt} = -\frac{\delta H[u,x]}{\delta x}$$
$$\frac{Dx}{Dt} = \frac{\delta H[u,x]}{\delta u} + (\text{forcing} + \text{dissipation}). \tag{19}$$

Now, the equation $DH/Dt=0$ defines an hypersurface in the (infinite-dimensional) space of states, whose intersection with the global attractor contains the set S of points of maximum energy. This set should be divided into subsets, one for each possible regime, which in the toy model of Lorenz are easily identified with the fractal sets of the two lobes. In the general case the regimes are not so clearly defined [21,11]. Since our approach is inevitably empirical and aimed at a possible practical application of energy-based long-term predictions to more realistic situations, the problem of defining quasistationary regimes can be afforded in an empiric way

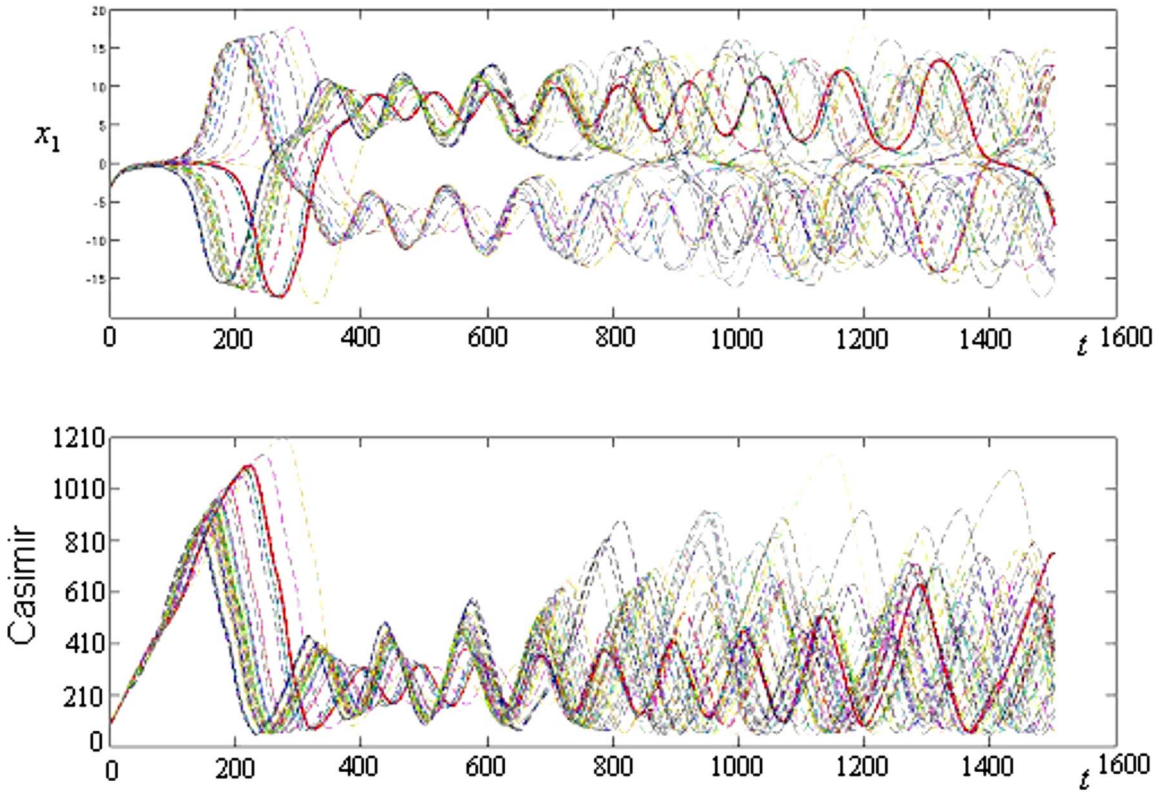

FIG. 13. (Color online) Evolution of x_3 (upper panel) and Casimir maximum (lower panel) starting from several initial conditions chosen within a corona of the same extension as before (Fig. 11), but centered at a random point on the attractor.

by considering a grid discretization in the space or a truncation in the spectral domain and applying the well-known empirical orthogonal function (EOF) analysis to the system's evolution (see, e.g., Ref. [18]), as is currently done in meteorology [22]. This analysis extracts a certain, hopefully small, number of preferred configurations capturing the main variability modes of the system. For simplicity, the analysis can be restricted to a fixed height or pressure level. Therefore, imagine that the fluid is the atmosphere and the domain of integration the whole spherical surface of the Earth. A

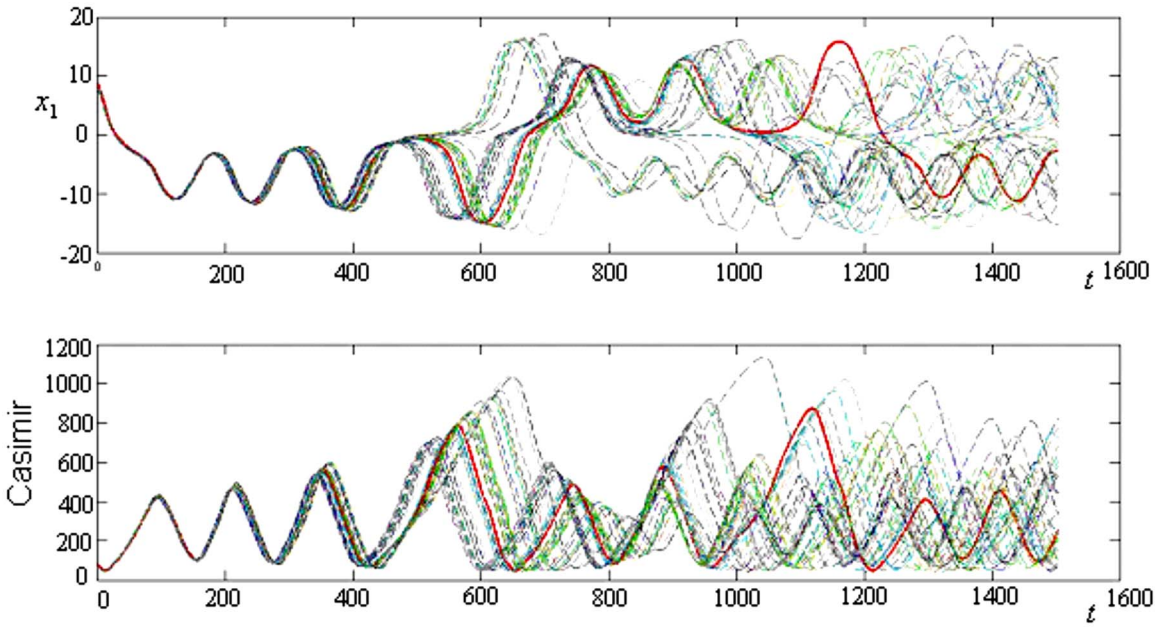

FIG. 14. (Color online) Evolution of x_3 (upper panel) and Casimir maximum (lower panel) starting from several initial conditions chosen within a corona of the same extension as before (Fig. 12) and centered at a different random point on the attractor.

good pressure level to study preferred configurations is the middle tropospheric level—i.e., the 500-hPa pressure level—and as far as we are concerned with climatic regimes, we can consider the monthly-averaged geopotential height anomalies. Denoting $\phi'_{i,k}$ the height anomaly for the ith grid point and the kth month, the preferred patterns, also called loading vectors, are obtained by taking the (first) orthonormal eigenvectors $\vec{E}_i$ of the covariance matrix

$$\hat{R}_{i,j} \equiv \frac{1}{N} \sum_{k=1\ldots N} \phi'_{i,k} \phi'_{j,k} \tag{20}$$

and multiplying it by the corresponding eigenvalue λ_i representing the fraction of the total variability [22]. A given height anomaly field can then be written as a linear combination

$$\vec{\phi}'_k = c_{1,k}\lambda_1 E_1 + c_{2,k}\lambda_2 E_2 + \cdots + \zeta, \tag{21}$$

where ζ indicates the residual state not represented by the first preferred patterns. As in Ref. [12], regimes can be found by studying the statistical distribution of states in the subspace spanned by the first EOFs. Now, it is possible to confine the maximum energy values, which can be extracted directly from the observed time series and with the time resolution of the meteorological analysis, to one of the identified regimes—of course, in the region of phase space where they are well defined.

It is sufficient, for this purpose, to retain only those values whose corresponding coefficients $c_{h,k}$ are simultaneously found within some appropriate intervals, which define a volume in the mentioned subspace. Note that, in this case, precise knowledge is not required of the regimes themselves, in particular of their boundaries, which are quite arbitrary and strongly dependent on the analysis method employed.

Having defined the set of maximum energy points for a given regime, it can be experimentally verified if a given range of maximum energies is associated with a qualitative future behavior, such as the transition to some other regime and the mean residence time within it. We note that the predictor parameter used in Ref. [12] is not sensitive to this latter feature.

It should be stressed that, of course, there is not any *a priori* reason why this correlation should be found in more realistic cases as in our toy models, but if so, an experimental mapping of these maximum energy ranges and the associated long-term behavior could become a powerful instrument, for example, in weather regime forecasting. In this respect, it is worth noting that the presence of a constant forcing has been tacitly assumed up to now. In the case of climate we have of course a time periodic variation of the intensity of solar radiation reaching a given area of the planet, and the energy maximum in a given regime strongly depends on the period of the year considered, so that this situation requires a specific investigation, even in the framework of the simple low-dimensional systems we have considered.

VI. CONCLUSIONS

In conclusion, the use of the Hamiltonian formalism applied to the Lorenz model leads to an interesting "physical" interpretation in terms of discretized orbits and (maximum-) energy levels. The resulting skeletal dynamics, which takes place on a simplified two-dimensional manifold, seems to capture the basic mechanism underlying dynamics and, in particular, regime transitions. Besides, we have classified up to ten maximum-energy shells in such a way that, starting from a point within one of them, the number of turns the system experiences in the other regime is precisely determined.

[1] E. N. Lorenz, J. Atmos. Sci. **20**, 130 (1963).
[2] H. F. Creveling, J. F. dePaz, J. Y. Baladi, and R. J. Schoenhal, J. Fluid Mech. **67**, 65 (1975).
[3] K. A. Robbins, Math. Proc. Cambridge Philos. Soc. **82**, 309 (1977).
[4] J. A. Yorke and E. D. Yorke, J. Stat. Phys. **21**, 263 (1979).
[5] S. Yuan and C. Wunsch, Phys. Fluids **17**, 066601 (2005).
[6] S. Corti, F. Molteni, and T. N. Palmer, Nature (London) **398**, 799 (1999).
[7] A. Provenzale and N. J. Balmforth, http//gfd.whoi.edu/proceedings/1998/PDF/antonello.pdf
[8] E. N. Lorenz, Bull. Am. Meteorol. Soc. **50**, 345 (1969).
[9] V. I. Arnold and B. A. Khesin, *Topological Methods in Hydrodynamics* (Springer, Berlin, 1998).
[10] T. N. Palmer, Bull. Am. Meteorol. Soc. **74**, 49 (1993).
[11] A. Deloncle, *et al.*, J. Atmos. Sci. **64**, 1619 (2007).
[12] D. Kondrashov, K. Ide, and M. Ghil, J. Atmos. Sci. **61**, 568 (2004).
[13] P. J. Morrison, Rev. Mod. Phys. **70**, 467 (1998).
[14] V. Zeitlin, Phys. Rev. Lett. **93**, 264501 (2004).
[15] E. Kalnay, *Atmospheric Modeling, Data Assimilation and Predictability* (Cambridge University Press, Cambridge, England, 2003).
[16] A. Pasini and V. Pelino, Phys. Lett. A **275**, 435 (2000).
[17] A. Pasini and V. Pelino, Phys. Lett. A **291**, 389 (2001).
[18] V. Pelino and F. Maimone (unpublished).
[19] J. E. Marsden and T. Ratiu, *Introduction to Mechanics and Symmetry* (Springer, Berlin, 1994).
[20] R. Salmon, *Lectures on Geophysical Fluid Dynamics* (Oxford University Press, Oxford, 1998).
[21] F. Selten, J. Atmos. Sci. **52**, 915 (1995).
[22] M. Ghil, *et al.*, Rev. Geophys. **40**, 1003 (2002).